# Surface Electronic Structure and Mechanical Characteristics of Copper−Cobalt Oxide Thin Film Coatings: Soft X-ray Synchrotron Radiation Spectroscopic Analyses and Modeling

Amun Amri,[†,#] Zhong-Tao Jiang,*[,†] Parisa A. Bahri,[†] Chun-Yang Yin,*[,⊥] Xiaoli Zhao,[§] Zonghan Xie,[§,||] Xiaofei Duan,[‡] Hantarto Widjaja,[†] M. Mahbubur Rahman,[†] and Trevor Pryor[†]

[†]School of Engineering and Information Technology, Murdoch University, Murdoch 6150 WA, Australia
[‡]School of Chemistry, The University of Melbourne, Melbourne VIC 3010, Australia
[§]School of Engineering, Edith Cowan University, Joondalup WA 6027, Australia
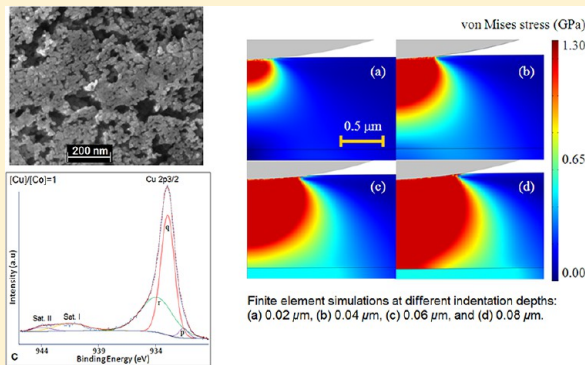[||]School of Mechanical Engineering, University of Adelaide, Adelaide SA 5005, Australia
[⊥]Chemical and Analytical Sciences, Murdoch University, Murdoch 6150 WA, Australia
[#]Department of Chemical Engineering, Riau University, Pekanbaru, Indonesia

**S** *Supporting Information*

**ABSTRACT:** Novel copper−cobalt oxide thin films with different copper/cobalt molar ratios, namely, $[Cu]/[Co]$ = 0.5, 1, and 2, have been successfully coated on aluminum substrates via a simple and cost-effective sol−gel dip-coating method. Coatings were characterized using high resolution synchrotron radiation X-ray photoelectron spectroscopy (SR-XPS) and near edge X-ray absorption fine structure (NEXAFS) spectroscopy, in combination with nanomechanical testing and field emission scanning electron microscopy (FESEM). The surfaces of both $[Cu]/[Co]$ = 0.5 and 1 samples consisted primarily of fine granular nanoparticles, whereas the $[Cu]/[Co]$ = 2 has a smoother surface. The analyses reveal that the increase of copper concentration in the synthesis process tends to promote the formation of octahedral $Cu^{2+}$ which minimizes the development of octahedral $Cu^+$, and these octahedral $Cu^{2+}$ ions substitute the $Co^{2+}$ site in cobalt structure host. The local coordinations of Co, Cu and O are not substantially influenced by the change in the copper to cobalt concentration ratios except for the $[Cu]/[Co]$ = 2 coating where the local coordination appears to slightly change due to the loss of octahedral $Cu^+$. The present film coatings are expected to exhibit good wear resistance especially for the $[Cu]/[Co]$ = 1.0 sample due to its high hardness/elastic modulus ($H/E$) ratio. Finite element modeling (FEM) indicated that, under spherical loading conditions, the high stress and the plastic deformation were predominantly concentrated within the coating layer, without spreading into the substrate.

von Mises stress (GPa)

Finite element simulations at different indentation depths: (a) 0.02 μm, (b) 0.04 μm, (c) 0.06 μm, and (d) 0.08 μm.

## INTRODUCTION

Copper cobalt mixed oxides ($Cu_xCo_yO_z$) such as $Cu_xCo_{3-x}O_4$ spinel-type and $CuCoO_2$ delafossite-type have attracted much attention and have been studied for a wide range of applications, such as oxygen evolution reactions (OER), the Fischer−Tropsch process, the synthesis of syngas-based alcohol, and as thermoelectric materials.[1−14] Such intensive focus is attributed to their high stabilities and high surface catalytic activities, good corrosion resistance, cost-effectiveness, and availabilities.[13,14] Many studies have revealed their physicochemical, electrochemical, magnetic, conducting, and thermal properties,[6,8,15−17] all of which are essential to afford functionalities and enhance application performances for these materials.

Physicochemical properties of copper−cobalt oxides such as their surface morphologies and surface electronic structures play an important role in governing electrocatalytic reactions or thermoelectric applications. For spinel electrocatalysis, it was reported that the mixed oxidation states of the cations placed in the octahedral sites (the external sites) are the main contributing factor in an increase of the electrical conductivity that facilitates the adsorption of the oxygen ($O_2$ gas or $OH^-$ ions) by providing donor−acceptor levels (d orbitals) for chemisorption, which in turn enhances electrocatalyst activity.[6] On the other hand, it has been well established that the distribution of the mixed cationic valences, which is the key determinant of catalytic activity and other physicochemical properties, is erratic because the distribution is strongly

influenced by the preparation method, i.e., the chemical nature and the compositions of the precursors, as well as the annealing atmosphere.[6,8,13] For delafossite, the mixed cationic valences are also critical in determining the high electrical conductivity. Beekman et al.[12] characterized the delafossite-type of $CuCoO_2$ prepared by ion exchange (metathesis) solid-state reaction between CuCl and $LiCoO_2$. They found that the electrical transport and magnetic susceptibility data for polycrystalline $CuCoO_2$ were consistent with formal charge assignments of $Cu^+$ and $Co^{3+}$ for the transition metal constituents and corroborated recent density functional theory calculations for this material.

Mechanical properties such as hardness ($H$), elastic modulus ($E$), and elastic strain to failure, which is related to the ratio of hardness and elastic modulus ($H/E$), are the important parameters required to estimate the wear resistance of nanostructured surfaces or coatings. The hardness itself is a good measure of resistance against abrasive wear; however, when taking into account the presence of plastic deformation mechanisms, the $H/E$ ratio is a more suitable parameter.[18] The mechanical properties of copper−cobalt oxides seem rarely to be studied. However, generally metal oxides show stability at high temperatures in air, are inert, and do not interdiffuse at working temperatures. In fact, some metal oxides such as alumina, chromia, and titania exhibit high hardness and high elastic modulus.[19−21] However a material with a high hardness and a lower elastic modulus is deemed to have a better toughness when plastic deformation is dominant, and is therefore better suited for optimizing the wear resistance of "real" industrial surface materials.[18] Hence by lowering the elastic modulus while maintaining hardness, an increase of the resistance against cracking should be achieved.

Recently we reported our work on copper−cobalt oxide thin film coatings on the top of highly reflective aluminum substrates using a customized, and yet, cost-effective sol−gel dip-coating method.[22,23] The new coatings demonstrated distinct optical properties with promising prospects for solar selective absorber application. Details regarding the metal oxidation states as well as the mechanical properties of these coatings are, nonetheless, rather sketchy and currently lacking even though they are vital for design optimization purposes. To address this issue, we have thus used a holistic approach to comprehensively determine the surface morphology, electronic structure, and its local coordination as well as the mechanical properties of these copper−cobalt oxide thin film coatings. To this end, field emission scanning electron microscopy (FESEM), high resolution synchrotron radiation X-ray photoelectron spectroscopy (SR-XPS) in combination with the synchrotron-based near edge X-ray absorption fine structure (NEXAFS) spectroscopy, and mechanical nanoindentation analysis have been employed for further characterization. As the deposited coating exhibits nanosized grain-like morphology with superior wear-resistant characteristics compared to the aluminum substrate, we further use finite element modeling (FEM) to complement the existing experimental data and to establish its load-bearing ability.

## EXPERIMENTAL SECTION

**Preparation of Thin Film Coatings.** Copper(II) acetate monohydrate ($Cu(OOCCH_3)_2 \cdot H_2O$, Alfa Aesar, 98%), cobalt-(II) chloride ($CoCl_2 \cdot 6H_2O$, APS Chemical, >99%), propionic acid ($C_2H_5COOH$, Chem Supply, 99%), and absolute ethanol (Merck) were used as received. The highly reflective

commercial aluminum material (Anofol, size $2 \times 4$ cm$^2$) was used as the substrate.

Copper(II) acetate monohydrate and cobalt(II) chloride (0.125 to 0.3 M) were mixed in absolute ethanol using propionic acid as the complexing agent to produce solutions with $[Cu]/[Co]$ concentration ratios of 0.5, 1, and 2. The solutions were then stirred for 2 h in sealed glass containers at room temperature. The solutions were deposited on aluminum substrates via dip-coating at a withdrawal rate of 120 mm/min with relative humidity being controlled below 55%. The samples were then heated on a hot plate at 150 °C for 10 s. The dip-heating cycles were conducted four times before final annealing in a furnace at 500 °C for 1 h. For nanoindentation analysis, thicker coatings were fabricated by more dip-heating cycles (30 times) to minimize substrate effects. The annealing process was conducted at a heating rate of 50 °C/min. The furnace was subsequently switched off to allow cooling for 10 min before finally being transferred to a desiccator.

**Characterizations.** The surface morphologies of the thin film samples were analyzed using FESEM (Zeiss Neon 40EsB). Prior to analysis, the sample was mounted on the substrate holder using carbon tape and sputter-coated with platinum to reduce any charging effects. InLens detectors were used at magnifications of 1 $\mu$m and 200 nm with an aperture size of 30 $\mu$m and, using an extra high tension voltage field emission gun, was set at 5 and 10 kV.

SR-XPS and NEXAFS analyses were conducted at the soft X-ray beamline at the Australian Synchrotron facility under storage ring operation of 200 mA and 3 GeV. The beamline was equipped with a collimated light plane grating monochromator SX700 with 1200 lines/mm plane grating. The samples were mounted on a stainless steel sample holder using adhesive carbon tapes and characterized under a background pressure of $1 \times 10^{-10}$ Torr in the analysis chamber. The photon energy used was 1253.6 eV. The copper, cobalt, and oxygen X-ray NEXAFS absorptions were measured in auger electron yield (AEY) mode with a channeltron facing the sample positioned 30° above the incoming beam and by monitoring drain current. To avoid an erroneous interpretation of the results, the obtained spectra were normalized by dividing the signal with the photon flux incident ($I_0$) which was monitored using a gold mesh. The samples were characterized at a step size of 0.1 eV over the energy region 920−980, 770−820, and 520−570 eV for Cu L-edge, Co L-edge, and O K-edge, respectively. The Co 2p, Cu 2p, and O 1s photoelectron lines were measured in XPS mode. The data were processed using SPECS (V2.75-R25274) and CasaXPS (V.2.3.15) software.

The mechanical properties of the film coatings were analyzed using a nanoindentation workstation (Ultra-Micro Indentation System 2000, CSIRO, Sydney, Australia), equipped with a Berkovich indenter.[24] The area function of the indenter tip was calibrated using a standard fused silica specimen. Samples with thicker coating layers, typically >1.5 $\mu$m, were fabricated for the experiments to minimize the substrate effect during measurement. Nanoindentation was conducted under load control with a maximum load of 2.0 mN, under which the maximum penetration depth was found to be less than 10% of the film thickness. This ensured that only the film properties were measured. For each test, 10 incremental and 10 decremental steps were used, respectively. Twenty indentations were performed for each sample.

Finite element modeling (FEM) was used to map the stress distribution within the coating and the substrate under
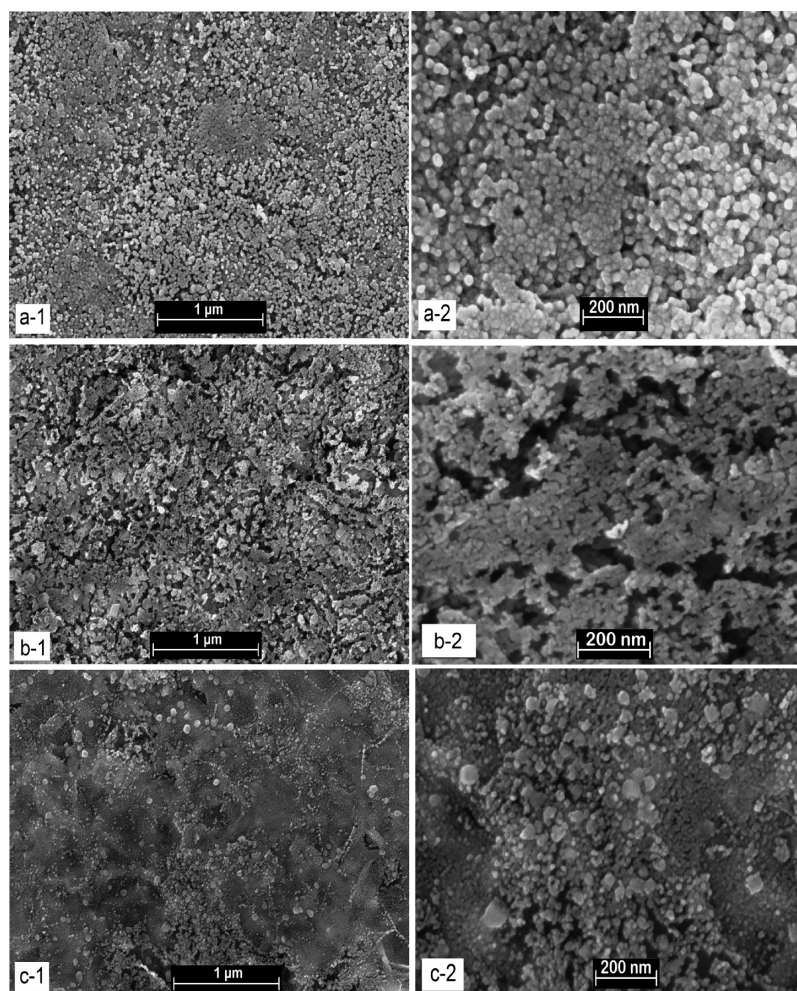
**Figure 1.** Surface morphologies of copper−cobalt oxide coatings synthesized using (a) [Cu]/[Co] = 0.5, (b) [Cu]/[Co] = 1, and (c) [Cu]/[Co] = 2.

spherical-tip indentation to assess the mechanical response of the coating system to external loading. Mechanical properties of the coating system, obtained from the nanoindentation tests, were used as input parameters. The simulations were performed using COMSOL Multiphysics Ver. 3.5a software. A two-dimensional (2D) axisymmetric model was generated with the loading direction along the axial $z$ axis. Details on the model setup are similar to our previous work,[25,26] and they are described briefly here. The model consists of a coating (1 $\mu$m thick) deposited on top of aluminum substrate (49 $\mu$m thick), loaded under a spherical tipped indenter with a radius of 5 $\mu$m. The simulation block is a rectangle measuring 50 × 50 $\mu$m. Time-dependent deformation behaviors, such as creep, as well as surface roughness and contamination were not considered in our simulations. The contact between the indenter and the sample is assumed to be frictionless. The boundary conditions are described below. The bottom ($z = -50\ \mu$m) is fixed in the $z$ direction, while the right edge of the block ($x = 50\ \mu$m) is fixed in the $x$ direction. The axisymmetric axis is placed on the left edge of the simulation block ($x = 0$) to generate 3D effects. The tip of the indenter was located at $z = 0\ \mu$m at the beginning of the simulation. The indentation loading process is simulated as downward movements in successive steps of 0.01 $\mu$m each, from 0 to 0.12 $\mu$m.

## ■ RESULTS AND DISCUSSION

**Surface Morphology.** Figure 1, panels a-1, b-1, and c-1, shows the surface morphologies of copper−cobalt oxide thin films synthesized using different copper to cobalt concentrations ratios at the 1 $\mu$m scale. Generally, the surfaces exhibit coarse surface morphologies except for the [Cu]/[Co] = 2 sample which has a smoother surface (Figure 1c-1). The smoother surface exhibited by the [Cu]/[Co] = 2 sample is due to increased agglomeration to form a dense and more uniform surface structure. Overall, the surface roughness of the copper−cobalt system appears to be influenced by copper content, that is, the higher the copper concentration, the smoother the resulting surface would be and vice versa. With closer examination (Figure 1, panels a-2, b-2, and c-2), the surfaces consist of grain-like nanoparticles with sizes ca. 10−60 nm. For [Cu]/[Co] = 1, the particles appear to agglomerate to form a coral-like morphology embedded within pores/trenches (Figure 1b-2). Interestingly, relatively homogeneous particle sizes and arrangement are observed for [Cu]/[Co] = 0.5 as compared to [Cu]/[Co] = 1, implying a more pronounced particle agglomeration for the latter. Such morphologies were previously reported by other researchers[7,13,27] for their porous copper−cobalt oxide layers synthesized via thermal decomposition of copper and cobalt nitrate precursors for electrocatalytic application. Marsan and co-workers[7] suggested that
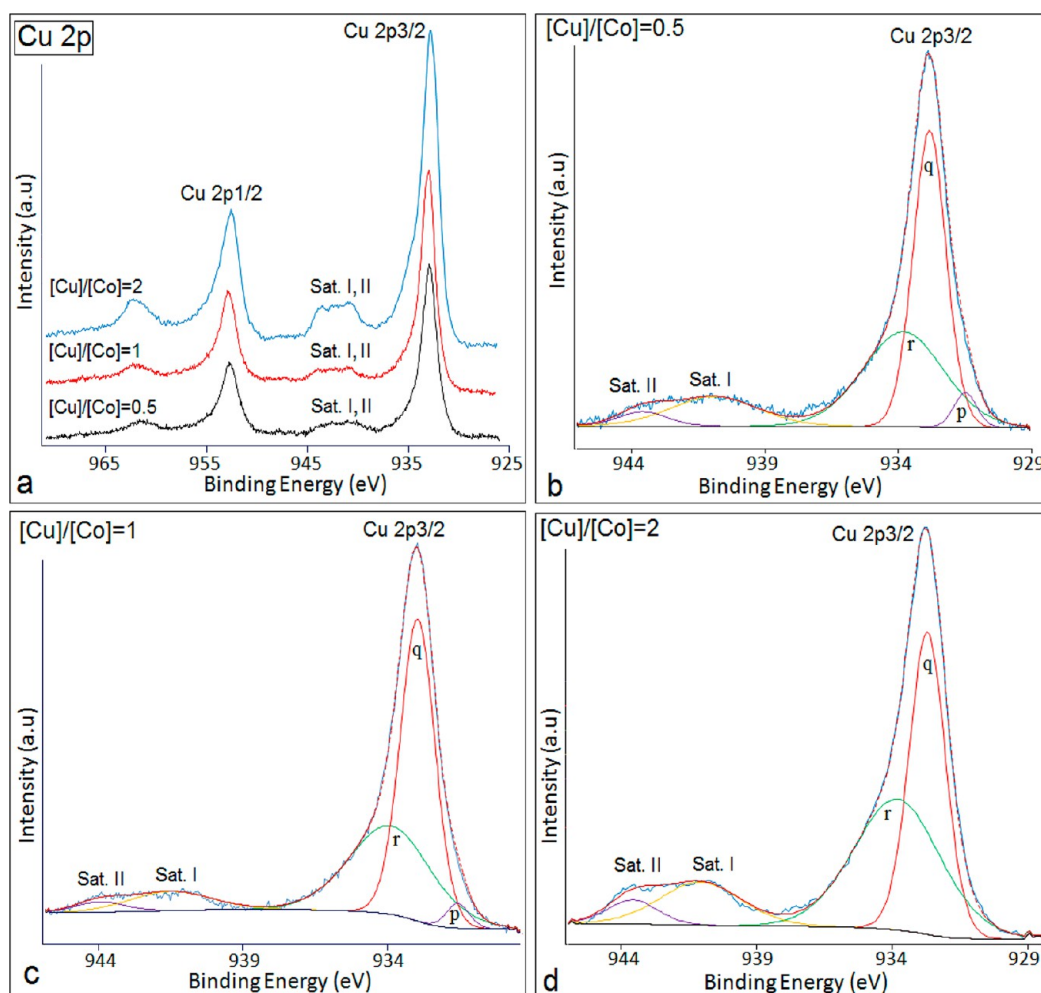
**Figure 2.** (a) Cu 2p SR-XPS spectra of copper−cobalt thin film coatings synthesized using different [Cu]/[Co] concentration ratios and (b−d) decoupling of their corresponding Cu $2p_{3/2}$ peak.

**Table 1. Binding Energies and the Percentage Compositions Derived from the Decoupling of Cu $2p_{3/2}$ peak and Its Satellites in the Copper−Cobalt Film Coatings**

| film coatings | binding energy and the percentage of the components of the Cu $2p_{3/2}$ photoelectron line | | | binding energy and the percentage of satellites | |
|---|---|---|---|---|---|
| | p | q | r | satellite I | satellite II |
| [Cu]/[Co] = 0.5 | 931.5 eV (3.7 at. %) | 932.8 eV (45.5 at. %) | 933.8 eV (35.7 at. %) | 940.9 eV (11.9 at. %) | 943.6 eV (3.2 at. %) |
| [Cu]/[Co] = 1 | 931.5 eV (2.8 at. %) | 932.9 eV (51.4 at. %) | 933.9 eV (35.8 at. %) | 941.5 eV (7.6 at. %) | 944 eV (2.5 at. %) |
| [Cu]/[Co] = 2 | | 932.7 eV (40.6 at. %) | 933.8 eV (42.0 at. %) | 941.0 eV (13 at. %) | 943.6 eV (4.4 at. %) |
| attributions: | octahedral Cu$^+$ | tetrahedral Cu$^+$ | octahedral Cu$^{2+}$ | paramagnetic Cu$^{2+}$ | paramagnetic Cu$^{2+}$ |

the porous/rough morphology of the copper−cobalt oxide surface was attributed to the higher evolution of gas volumes ($NO_2$ and $O_2$) during the decomposition of the concentrated nitrate coating. In line with their analysis, the observed morphologies of our copper−cobalt oxide coatings could be attributed to the evolution of $O_2$ from the high temperature decomposition of copper and/or cobalt oxides which ultimately form the copper−cobalt oxide.[28,29]

**Synchrotron Radiation XPS Study.** The high resolution SR-XPS was used to afford detailed information regarding the electronic structure of the thin film coatings. Figure 2 shows the Cu 2p SR-XPS spectra and the decoupling of Cu $2p_{3/2}$ peaks of the copper−cobalt oxide film synthesized using different concentration ratios. In each spectrum, the two main peaks of Cu $2p_{3/2}$ and Cu $2p_{1/2}$ and the satellites on the high energy

side of each of the main peaks can be observed (Figure 2a). The presence of these satellites represents evidence of an open $3d^9$ shell of Cu$^{2+}$.[30] Qualitatively, in each spectrum, the binding energy difference between Cu $2p_{1/2}$ and Cu $2p_{3/2}$ which is around 19.9 eV, and the shake satellite on the high energy side of the Cu $2p_{3/2}$ peak, confirm the presence of Cu$^{2+}$ ions. The shorter separation between the Cu $2p_{3/2}$ line and its satellite peak, and the higher value of satellite intensity to Cu $2p_{3/2}$ main peak intensity ($I_{sat}/I_{main}$) ratio, signify a decrease in the covalent character of the Cu−O bond in copper−cobaltite as compared to CuO.[13] Relatively higher intensity of Cu 2p satellites in the sample with a [Cu]/[Co] = 2 also indicates the higher number of Cu$^{2+}$ ions which are not incorporated into the copper−cobalt spinel structure compared with the other two concentration ratios. The copper−cobalt spinel atomic structures with
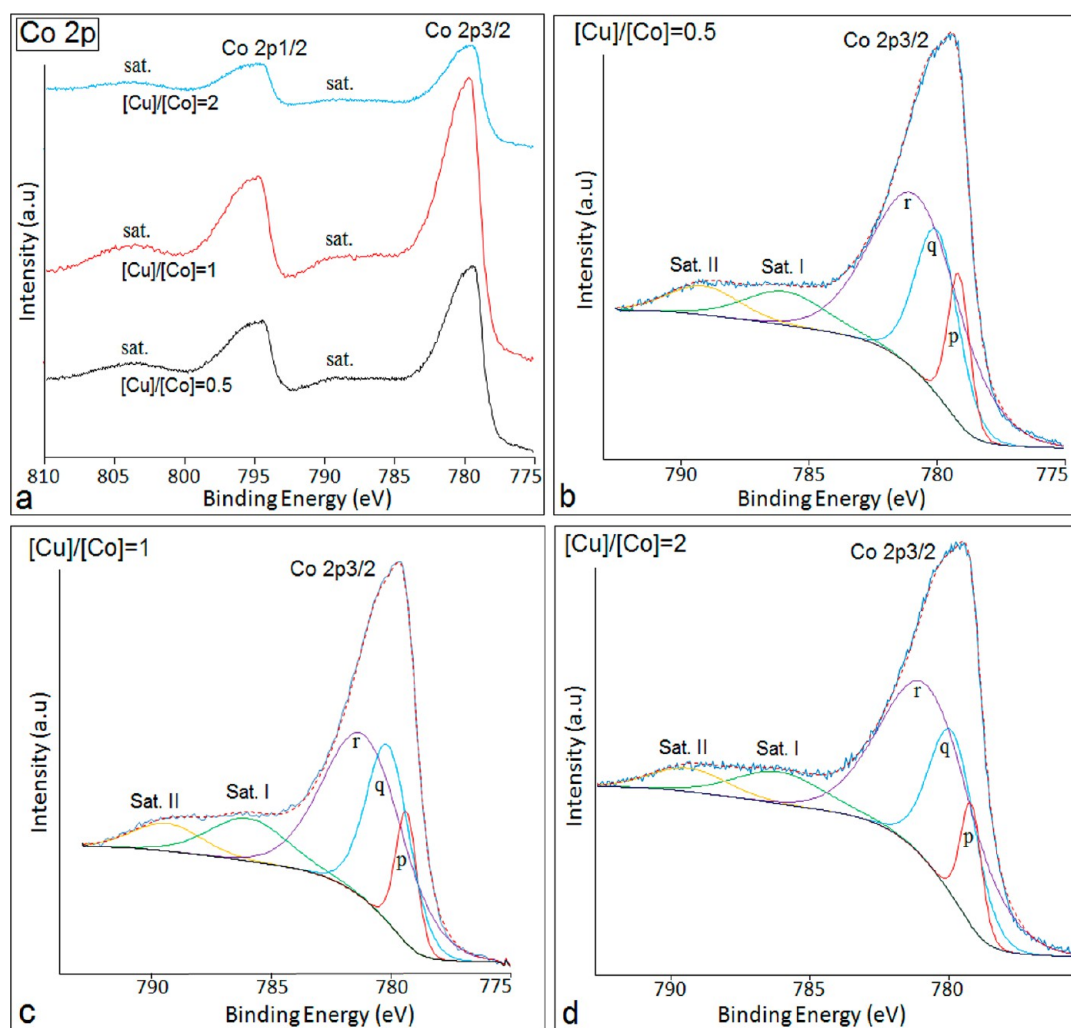
**Figure 3.** (a) Co 2p SR-XPS spectra of copper−cobalt thin film coatings synthesized using different [Cu]/[Co] concentration ratios and (b−d) decoupling of their corresponding Co 2p$_{3/2}$ peak.

different atomic compositions can be found in the Supporting Information.

The decoupling of Cu 2p$_{3/2}$ peak and its satellite in each coating is shown in Figure 2b−d. The decoupling provides five curve-fitting components except for the sample with [Cu]/[Co] = 2 which does not contain any component below the binding energy of 932 eV (Figure 2d). The quantitative analysis results are presented in Table 1. It is commonly recognized that the Cu 2p$_{3/2}$ photoelectron peaks at ca. 933.8−933.9 eV are due to the Cu$^{2+}$. Many researchers[23] identify that the Cu 2p$_{3/2}$ photoelectron peak at ca. 932.7−932.9 eV is attributed to the tetrahedral Cu$^+$ with its counterpart peak from the octahedral Cu$^+$ located below the tetrahedral one. From Table 1, it can be observed that the tetrahedral Cu$^+$ is the more prominent oxidation state in each sample except for the [Cu]/[Co] = 2 sample whereby the numbers of tetrahedral Cu$^+$ and octahedral Cu$^{2+}$ are relatively balanced. The increase of copper content tends to promote the formation of octahedral Cu$^{2+}$ and to reduce the formation of octahedral Cu$^+$. It is shown that, for the [Cu]/[Co] = 2 sample, there is no reduction of Cu$^{2+}$ in the octahedral environment compared to the other two samples. In addition, the absence of octahedral Cu$^+$ implies that there are fewer amounts of typical monophasic Cu−Co mixed oxides in the coating for the [Cu]/[Co] = 2 sample compared to the

other two samples.[13] The presence of Cu$^{2+}$ ions in an octahedral environment is in contrast with the copper spinel structure, where Cu$^{2+}$ predominantly occupies the tetrahedral sites. This suggests that in the copper−cobalt system, the Cu$^{2+}$ ions themselves are 'guests' which partially substitute the tetrahedral Co$^{2+}$ in the cobalt structure host.[23] Based on these observations, it can be suggested that in the copper−cobalt system with a [Cu]/[Co] = 2, the elevated concentrations of copper have increased the competitiveness of octahedral Cu$^{2+}$ ions, which facilitates occupation of the Co$^{2+}$ sites in the cobalt structure host while minimizing the driving-force of Cu$^{2+}$ to undergo reductions.

The profile of the Co 2p spectra is shown in Figure 3a. In each spectrum, the two main peaks are attributed to Co 2p$_{3/2}$ and Co 2p$_{1/2}$, and the weak satellites located on the high energy side of each of these main peaks are also found. Qualitatively, the presence of satellite on the high energy side of the Co 2p$_{3/2}$ peak indicates the presence of Co$^{2+}$ ions. The Co 2p$_{3/2}$ peak and Co 2p$_{1/2}$ peaks separated by a spin−orbit splitting of ~15 eV correspond to the mixed Co$^{2+}$ and Co$^{3+}$ ions, while the weak intensity satellite located in between the Co 2p$_{3/2}$ and Co 2p$_{1/2}$ indicates that the Co ions are present in a partial spinel-type lattice arrangement. The weak satellite structures are the characteristic of spinel structures in which 3$^+$ cations occupy

**Table 2. Binding Energies and the Percentage Compositions Derived from the Decoupling of Co $2p_{3/2}$ Peak and Its Satellites in the Copper−Cobalt Film Coatings**

| film coatings | binding energy and the percentage of the components of Co $2p_{3/2}$ photoelectron line | | | binding energy and the percentage of satellites | |
|---|---|---|---|---|---|
| | p | q | r | satellite I | satellite II |
| [Cu]/[Co] = 0.5 | 779.2 eV (10.3 at. %) | 780 eV (22.9 at. %) | 780.8 eV (51.4 at. %) | 785.9 eV (8.8 at. %) | 789.1 eV (6.5 at. %) |
| [Cu]/[Co] = 1 | 779.4 eV (9.7 at. %) | 780.1 eV (26.6 at. %) | 781.1 eV (45.8 at. %) | 786 eV (11.5 at. %) | 789.3 eV (6.5 at. %) |
| [Cu]/[Co] = 2 | 779.2 eV (8.3 at. %) | 779.9 eV (24.5 at. %) | 780.7 eV (52.5 at. %) | 786.1 eV (9.1 at. %) | 789.4 eV (5.6 at. %) |
| attributions | octahedral $Co^{3+}$ | mixed $Co^{2+,3+}$ | tetrahedral $Co^{2+}$ | paramagnetic $Co^{2+}$ | paramagnetic $Co^{2+}$ |
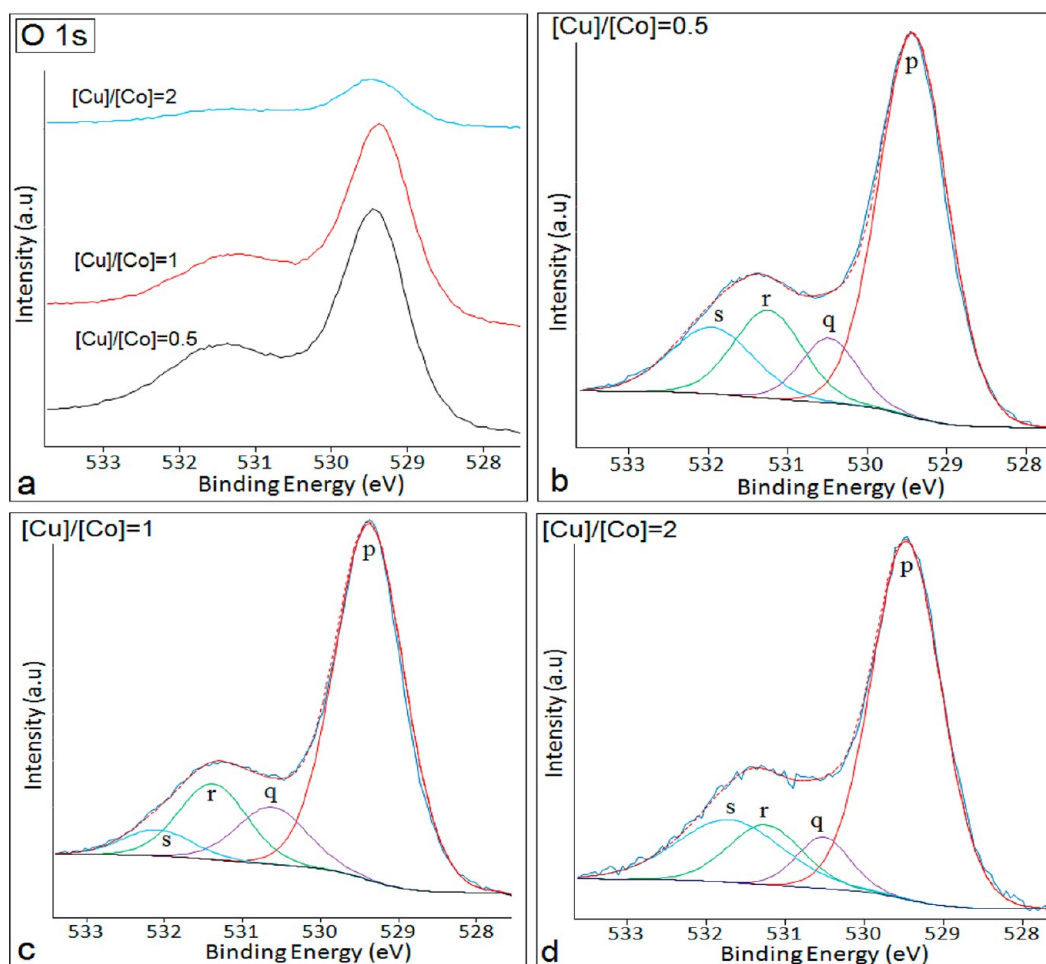


**Figure 4.** (a) O 1s SR-XPS spectra of copper−cobalt thin film coatings synthesized using different [Cu]/[Co] ratios and (b−d) decoupling of their corresponding O 1s peaks and shoulders.

octahedral lattice sites with diamagnetic, filled $t_{2g}$ and empty $e_g$ levels, and $2^+$ cations are in tetrahedral sites.[31] The observed asymmetry in the Co $2p_{1/2}$ peak confirms the existence of both $Co^{2+}$ and $Co^{3+}$ ions.

In every spectrum, the decoupling of the Co $2p_{3/2}$ peak and the satellite on the high energy side of this peak provides five curve-fitting components (Figure 3b−d). The binding energy and the percentage of each component are tabulated in Table 2. The peaks in the region of 779.2−780.1 eV are mostly due to $Co^{3+}$ in an octahedral environment and mixed $Co^{2+,3+}$ bonding states. Due to the covalence and final state effects, the binding energy of $Co^{2+}$ is higher than that of $Co^{3+}$, and it is found mostly above 780.1 eV with a characteristic shakeup satellite.[23,32] In Table 2, it can be seen that, in all samples, the tetrahedral $Co^{2+}$ ions dominate. However, in a copper−cobalt mixed oxide system, the $Co^{2+}$ ions are partially

substituted by $Cu^{2+}$ ions, forming a lower crystallization of copper−cobalt spinel particles.[8] If $Cu^{2+}$ ions and octahedral $Co^{3+}$ ions are present in the copper−cobalt oxide system, then the oxide could be represented by $Cu^{2+}Co_2^{3+}O_4$, a form of copper−cobalt oxide structure.

Figure 4 shows the O 1s SR-XPS spectra of copper−cobalt oxide film coatings and the corresponding curve-fitting resulting from the decoupling of the 1s peak. The O 1s spectrum exhibits a strong peak with a shoulder at the high binding energy side of O 1s peak, except for the [Cu]/[Co] = 2 sample, where a relatively lower intensity peak is identified (Figure 4a). The apparent shoulder at the higher energy side of the O 1s main peak is a typical feature of copper−cobalt mixed oxides.[8] The decoupling of O 1s photoelectron spectrum in each sample results in four curve-fittings grouped into three components (Figure 4b-d). The curve-fitting peaks at binding energy (BE)

at around 529.4−529.5 eV (labeled "p") are mostly attributed to the lattice $O^{2-}$ in a $Co_3O_4$ spinel structure. The presence of this spinel as the main structure reaffirms that in the mixed copper−cobalt system here the cobalt oxide itself becomes the spinel host with copper ions as "guests", and then a copper−cobalt oxide spinel structure is formed as elucidated earlier.

The curve-fitting peaks at BE in the range of 530.4−531.4 eV (labeled "q" and "r") may be attributed to surface oxygen from a wide variety of species such as chemisorbed oxygen $O^-$, oxygen containing surface contamination, and/or OH-like species, as hydroxyl, carbonate groups, etc.[6,8,13,27,33−35] while the curve-fitting peaks at BE above 531.4 eV (labeled "s") could be assigned to subsurface $O^-$ species.[36−38] Dupin et al.[37] suggested that the subsurface (bulk structure near the surface) oxygen ions had lower electron density than the lattice $O^{2-}$ ions. They could be associated with sites where the coordination number of oxygen ions was smaller than in a regular site, with a higher covalence of the M−O bonds.[37]

**Synchrotron-Based NEXAFS Study.** Further interfacial studies to detect the influence of copper to cobalt concentration ratios to the local coordination of the electronic structure were performed using synchrotron radiation NEXAFS spectroscopy. Figure 5 shows the Cu L-edge NEXAFS
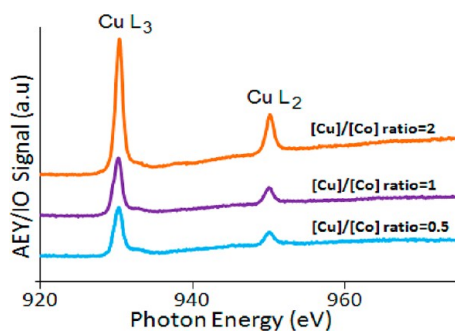
**Figure 5.** Cu $L_{2,3}$-edge NEXAFS in AEY mode spectra of copper−cobalt oxide thin film coatings.

absorption spectra in Auger Electron Yield (AEY) mode with monitoring photon flux incident ($I_0$). The AEY mode provides a better surface sensitivity compared to the TEY mode, as the latter detects the drain current for both surface and bulk material.[39] Two main peaks, i.e., Cu-$L_2$ and Cu-$L_3$, are observed at all spectra. All peaks and shoulders are found to exist around the same photon energy. Generally, it can be seen that there is no significant change in the spectral line-shapes with the change in copper and cobalt concentrations except for the [Cu]/[Co] = 2 sample where significantly higher peak intensities of Cu-$L_2$ and Cu-$L_3$ are observed. This indicates that the local environment of Cu remains relatively invariant in samples except for the [Cu]/[Co] = 2 sample.

The Cu-$L_3$ and Cu-$L_2$ absorption peaks are observed at photon energies of ∼930.4 and 950.2 eV, respectively. These main peaks arise from the dipole transitions of the Cu $2p_{1/2}$ for $L_2$ and Cu $2p_{3/2}$ for $L_3$ into the empty d states.[40] The Cu-$L_3$ peak is more sensitive to the local environment than the Cu-$L_2$ peak, which can be attributed to the $Cu^{2+}$ ions.[41−45] This observation reinforces the conclusion arrived at in the previous XPS analysis that there would be changes in the local coordination if the copper/cobalt concentration ratio is higher than 1, due to the loss of octahedral $Cu^+$.

The absorption peaks of the Co $L_{2,3}$-edge NEXAFS spectra for copper−cobalt oxide film coatings in AEY mode are shown in Figure 6. Generally all spectra exhibit relatively similar line-
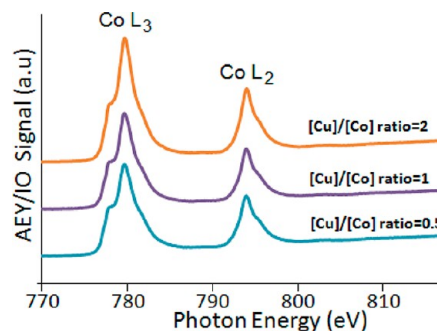
**Figure 6.** Co $L_{2,3}$-edge NEXAFS in AEY mode spectra of copper−cobalt oxide thin film coatings.

shapes and intensities which indicate that the local co-ordination of Co remains relatively unchanged in all samples. It has been known that the Co L-edge feature is sensitive to a change in electronic configuration; in particular, it will change drastically with the change in Co oxidation states and the spin-state transition.[46,47] Based on this evidence, the local environments of Co here are independent of the change to the copper to cobalt concentrations ratios.

In Figure 6, each spectrum has two main prominent peaks with shoulders. The Co-$L_3$ peak which has absorption at ∼779.6 eV has a shoulder on the low energy side with a shoulder corner at ∼777.8 eV and a thin shoulder/asymmetric behavior on the high energy side at an area of around 781.6 eV. Another absorption peak as Co-$L_2$ is found at 793.9 eV with a relatively more pronounced shoulder on the high energy side. In addition, their features show that the Co-$L_3$ peak form is relatively narrow with regard to the low spin state.[46] The distance separation between $L_3$ and $L_2$ peaks is around ∼14.3 eV, whereas no satellite peak between the $L_3$ and $L_2$ peaks can be found. These features are indicative of the presence of $Co^{3+}$. The thin shoulder on the high photon energy side of the Co-$L_3$ peak confirms that there is no presence of $Co^{4+}$ in the structure.[48] The low spin state is also confirmed by the branching ratio of the $L_2$ and $L_3$ peak intensities, namely $I(L_3)/[I(L_3) + I(L_2)]$, which are around 0.5−0.55 (below the statistical value) in each spectrum showing a low spin state $Co^{3+}$.[49,50] Gautam et al.[51] revealed that the similarity in form between the high energy side shoulder of Co-$L_3$ and Co-$L_2$ peaks was due to the Coulomb and exchange interaction of 2p core holes with the 3d electrons.

Figure 7 shows the O K-edge NEXAFS spectra for copper−cobalt film coatings in AEY mode. All spectra have a relatively similar trend and it is clearly evident that the local environments of O are relatively similar and they are relatively independent of the changes in copper to cobalt concentrations. The O K-edge main absorption peaks are found at photon energy values of around ∼530.5 and ∼542.4 eV.

The O K-edge NEXAFS feature can be used to investigate the hybridization of the metal 3d orbital with the host O 2p orbital. The O K-edge spectra in the binary metal mixed oxide involving the Co system emerge mainly due to the transition of the O 1s electron to the conduction band near the Fermi surface, which is dominated by the O 2p and transition metal 3d hybridized orbital.[52] In each spectrum (Figure 7), the peak

16463

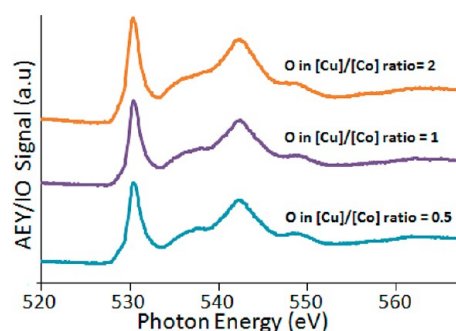dx.doi.org/10.1021/jp404841m | J. Phys. Chem. C 2013, 117, 16457−16467

**Figure 7.** O K-edge NEXAFS spectra in AEY mode for copper–cobalt oxide thin film coatings.

at ~530.5 eV is attributed to the hybridization of Co 3d states with O 2p states which is close to the conduction-band minimum and influenced by the density of unoccupied Co 3d states. Relatively sharp and narrow peaks at ~530.5 eV are due to the low spin configuration.[46] The peak at around 542.4 eV is attributed to the transitions of the nondispersive O $2p_z$ and $2p_{x+y}$. The shoulder on the low energy side of the 542.4 eV peak could be due to the presence of the O vacancies and Co, while the shoulder on the high energy side of this peak and the area above this shoulder are attributed to O 2p hybridized with Co 4 sp states and O 2p states that extend to a Co higher orbital, respectively.[51−53] The area between the two main peaks is attributed to O 2p hybridization with Co 3d states that form the bottom of the conduction band.[52] In the case of a copper–cobalt oxide system with cobalt as the host structure, these cobalt ionic structure features suggest that the copper ions, as guests, have an interaction with the cobalt host and that they are tetrahedrally coordinated with the ligand O atoms.[51]

**Nanoindentation.** The representative load–displacement curves obtained from the nanoindentation experiments on the different coating samples are shown in Figure 8. The elastic
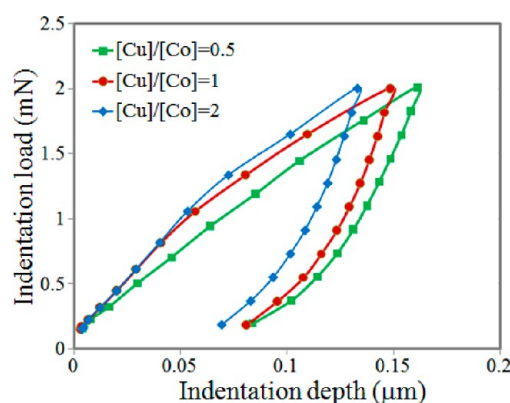


**Figure 8.** Load–displacement curves for the present coating samples.

modulus ($E$), hardness ($H$), and hardness to modulus ratio ($H/E$) values of the thin film coatings were derived from the nanoindentation results and are presented in Figure 9a–c, respectively. The sample with $[Cu]/[Co] = 2.0$ exhibits the highest average elastic modulus while the samples with $[Cu]/[Co] = 1$ and 0.5 show a lower average elastic modulus values with slightly differentiation (Figure 9a). In addition, it is evident that the elastic modulus of the three samples here is significantly lower than that of the aluminum substrate, which is consistent with our previous findings on coatings with similar
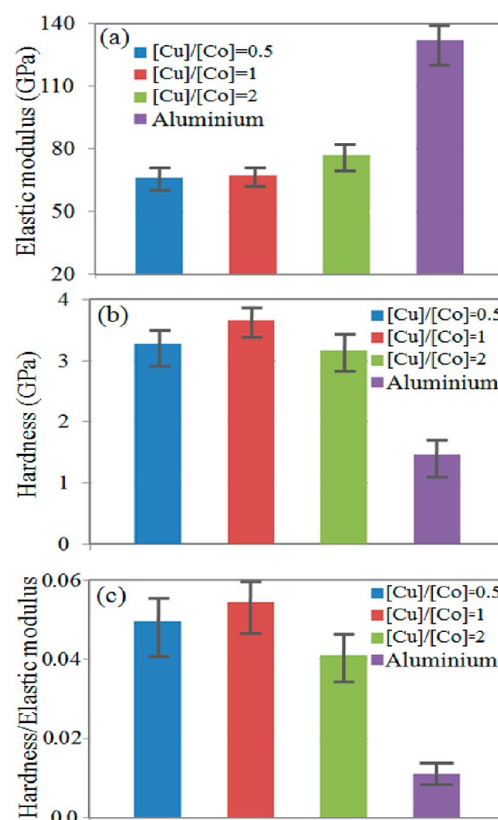


**Figure 9.** Mechanical properties of the as-deposited coatings derived from the nanoindentation tests: (a) elastic modulus. (b) hardness. and (c) $H/E$. The aluminum substrate is used for comparison.

compositions.[22] A different trend is shown by the hardness properties where the sample with the intermediate $[Cu]/[Co] = 1.0$ has the highest average hardness (~3.6 GPa) among all the three samples (Figure 9b). Interestingly, the hardness is about twice that of the aluminum substrate. As comparison, the other mixed metal oxide, such as the $Ca_3Co_4O_9$ ceramic developed for a thermoelectric application, had hardness of $H = 2.04−2.13$ GPa and elastic modulus of $E = 45.3−62.8$ GPa.[54]

The main factors governing the mechanical properties of nanostructure materials include structural composition and the chemical nature.[55] From the elastic modulus and the hardness results, the morphology and porosity factors in the surface of coatings as shown in the previous Surface Morphology section seem to have an influence on the mechanical properties, which is reflected by the fact that there is a spread of data points that results in an error ~10%. This could be because the porosities or densities are not uniform either in the surface or in the bulk. The increase of the copper constituent in the copper–cobalt oxide coating tends to increase the elastic modulus. In fact, it is widely known that the elastic modulus of cobalt metal is higher than the elastic modulus of copper metal, likewise in part of their metal oxides. If it is assumed that the composition in the bulk of the coating near the surface (at the depth of penetration achieved by the indenter) can be represented by the surface composition, then the elastic modulus of the copper–cobalt oxide could decrease with an increase of the copper constituent in the coating. A new mixed metal oxide has been formed that has different elastic modulus characteristics compared to the individual constituents. Further, using a similar route of synthesis, it could be estimated roughly that in the mixed copper–cobalt oxide thin film coatings, the coatings with a

16464

dx.doi.org/10.1021/jp404841m | *J. Phys. Chem. C* 2013, 117, 16457−16467

lower content of cobalt constituent would have a higher elastic modulus compared to the coatings containing a minimum amount of copper constituent.

The wear resistance of the coating can be evaluated using the $E$ and $H$ values obtained from the nanoindentation experiments. The $H/E$ ratio is considered to be an important parameter for predicting wear resistance.[18] Compared to the aluminum substrate, the present coatings are envisaged as having better wear resistance (Figure 9c), particularly for the $[Cu]/[Co] = 1.0$ sample which shows the highest $H/E$ value (0.055). The superior wear resistance exhibited by our coatings has direct implications in terms of sustaining performance and function of the optical devices during routine maintenance and service as mechanical contact can always be expected. For comparison, the wear resistance or the toughness of our coating here is better than reported values for other mixed metal oxides, for example $Ca_3Co_4O_9$ ceramic, had a reported value of $H/E$ of $0.03-0.04$.[54,56]

**Finite Element Modeling (FEM).** To investigate the load-bearing ability of the as-deposited coatings, FEM was conducted using the parameters listed in Table 3 as obtained

**Table 3. Mechanical Parameters Used for FEM Analysis**

| parameters (GPa) | [Cu]/[Co] = | | | aluminum |
|---|---|---|---|---|
| | 0.5 | 1.0 | 2.0 | |
| $E$ | 66 | 67 | 77 | 132 |
| $H$ | 3.3 | 3.7 | 3.2 | 1.455 |
| yield strength | 1.1 | 1.2 | 1.05 | 0.5 |

from our nanoindentation experiments. Simulation results for a coating synthesized using $[Cu]/[Co] = 1.0$ are shown in Figure 10, where the stress distribution under progressive loading is
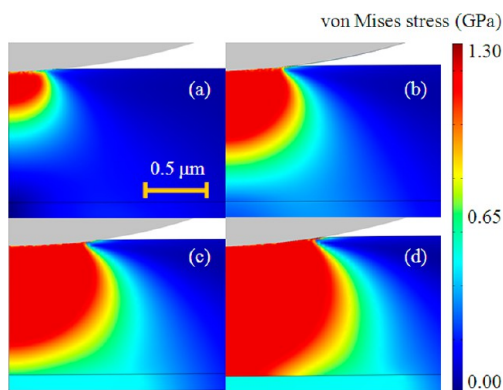
**Figure 10.** Stress distribution of the $[Cu]/[Co] = 1$ sample obtained from FEM simulations for different indentation depths: (a) 0.02, (b) 0.04, (c) 0.06, and (d) 0.08 $\mu$m.

presented. The concentrations of higher stress as well as the plastic zone were primarily restricted within the coating layer by up to an indentation depth of 0.08 $\mu$m. This is expected because all three coating layers have lower elastic modulus but higher hardness than that of the aluminum substrate, such that there is little plastic deformation within the aluminum substrate below the interface. As a result, the coating delamination is suppressed, which typically occurs at the interface between the coating and plastically deformed substrate during unloading.[57] Stress distributions for the other two coatings, i.e., $[Cu]/[Co] = 0.5$ and 2 samples, are similar to that of the $[Cu]/[Co] = 1$

sample, and hence, for brevity, they are not shown here. However, when the same loading is applied directly onto the Al substrate, a marked difference is observed, as shown in Figure 11, where the plastic zone of the loaded samples (coated and
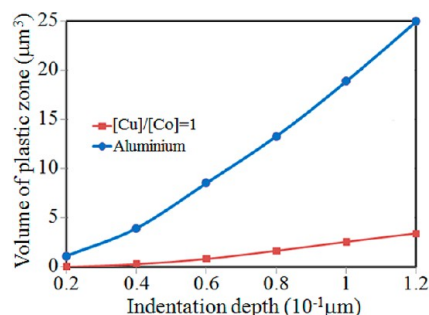
**Figure 11.** Change of the plastic zone size for the $[Cu]/[Co] = 1.0$ sample as compared to the aluminum under increasing load as derived from domain integration of the FEM results.

uncoated) are evaluated from FEM results using domain integration, and plotted against the indentation depth. The size of the plastic zone resulting from the same loading has increased 5−7 times, indicating a significant increase in the plastic deformation, which is detrimental to the integrity of the coating/substrate system. Hence in terms of load-bearing performance, improvement can be expected when the coating layer with higher $H/E$ is applied.

## CONCLUSIONS

Copper−cobalt oxide thin films with different compositions have been successfully deposited on aluminum substrates using a sol−gel dip-coating method and characterized via FESEM, SR-XPS, NEXAFS, and nanoindentation analyses. The surfaces of the $[Cu]/[Co] = 0.5$ and 1 samples were typically composed of granular nanoparticles, whereas the $[Cu]/[Co] = 2$ sample had a smoother surface. The SR-XPS analyses showed that the copper electronic structure consisted of octahedral $Cu^+$ (except for $[Cu]/[Co] = 2$), tetrahedral $Cu^+$ and octahedral and paramagnetic $Cu^{2+}$ oxidation states. The cobalt electronic structure comprised tetrahedral and paramagnetic $Co^{2+}$, mixed $Co^{2+,3+}$, and octahedral $Co^{3+}$ oxidation states, in which the tetrahedral $Co^{2+}$ was predominant. The oxygen electronic structure consisted of lattice, surface, and subsurface oxygen. The increase of copper concentration in the synthesis process tended to promote the formation of octahedral $Cu^{2+}$ which minimized the formation of octahedral $Cu^+$ as well as increased competitiveness of octahedral $Cu^{2+}$ ions to substitute the $Co^{2+}$ site in cobalt structure host. NEXAFS spectra revealed that the local environments of Co, Cu and O were not significantly influenced by the change in the copper to cobalt concentration ratios except for the $[Cu]/[Co] = 2$ sample where the local coordination appeared to slightly change due to the loss of octahedral $Cu^+$. Compared to the aluminum substrate, the present coatings have significantly improved wear resistance, particularly for the $[Cu]/[Co] = 1.0$ sample which shows the highest $H/E$ value (0.055). FEM modeling indicated that, under spherical loading conditions, the higher stress and the plastic deformation were primarily concentrated within the coating layer, without spreading further into the substrate. This would reduce the probability of delamination of the coating layer during unloading phase. Our findings can be used to aid in the engineering design of metal oxide coatings with much

higher wear-resistance for numerous industrial applications, such as optical coatings and solar-selective absorbers.

■ **ASSOCIATED CONTENT**

**Ⓢ Supporting Information**

Table S1 shows the number of atoms in a unit cell for $Cu_xCo_{3-x}O_4$ for various $x$ values. The XRD result shows that $Cu_xCo_{3-x}O_4$, known as copper−cobalt spinel, is cubic and has $Fd\bar{3}m$ (227) space group with lattice parameter $a \approx 8.11$ Å. The value of $x$ determines the proportion of copper to cobalt atoms in the spinel. For $x > 1.0$, the excess of the copper atoms forms CuO, thus spinel coexists with CuO[1,2]. Spinel crystals, $Cu_{.95}Co_{2.05}O_4$ (Figure S1), $Cu_{.56}Co_{2.44}O_4$ (Figure S2), and $Cu_{.27}Co_{2.73}O_4$ (Figure S3), have been modeled solely based on the space group and lattice parameter provided, using GaussView 5.0.8 software. This material is available free of charge via the Internet at http://pubs.acs.org.

■ **AUTHOR INFORMATION**

**Corresponding Author**

*Tel.: +61 8 9360 2867. E-mail: Z.Jiang@murdoch.edu.au (Z.-T.J.); C.Yin@murdoch.edu.au (C.-Y.Y.).

**Notes**

The authors declare no competing financial interest.

■ **ACKNOWLEDGMENTS**

■ **REFERENCES**

(1) Fujimoto, K.; Oba, T. Synthesis of $C_1$-$C_7$ Alcohols from Synthesis Gas with Supported Cobalt Catalysts. *Appl. Catal.* **1985**, *13*, 289−293.

(2) Baker, J. E.; Burch, R.; Golunski, S. E. Synthesis of Higher Alcohols Over Copper/Cobalt Catalysts: Influence of Preparative Procedures on the Activity and Selectivity of Cu/Co/Zn/Al Mixed Oxide Catalysts. *Appl. Catal.* **1989**, *53*, 279−297.

(3) Xiaoding, X.; Doesburg, E. B. M.; Scholten, J. J. F. Synthesis of Higher Alcohols from Syngas - Recently Patented Catalysts and Tentative Ideas on the Mechanism. *Catal. Today* **1987**, *2*, 125−170.

(4) S. Angelov, D. M. Carbon Monoxide Oxidation on Mixed Spinels $Cu_xCo_{3-x}O_4$ (0 < X < 1) in the Presence of Sulphur Compounds. *Appl. Catal.* **1985**, *16*, 431−437.

(5) Bonchev, R.; Zheleva, T.; Sevov, S. C. Morphological and Compositional Characterization of Copper-Cobalt Spinel Made by Mechanochemical Reactions. *Chem. Mater.* **1990**, *2*, 93−95.

(6) Gautier, J. L.; Trollund, E.; Ríos, E.; Nkeng, P.; Poillerat, G. Characterization of Thin $CuCo_2O_4$ Films Prepared by Chemical Spray Pyrolysis. Study of Their Electrochemical Stability by Ex-situ Spectroscopic Analysis. *J. Electroanal. Chem.* **1997**, *428*, 47−56.

(7) Marsan, B.; Fradette, N.; Beaudoin, G. Physicochemical and Electrochemical Properties of $CuCo_2O_4$ Electrodes Prepared by Thermal Decomposition for Oxygen Evolution. *J. Electrochem. Soc.* **1992**, *139*, 1889−1896.

(8) Koninck, M. D.; Poirier, S.-C.; Marsan, B. $Cu_xCo_{3-x}O_4$ Used as Bifunctional Electrocatalyst. *J. Electrochem. Soc.* **2006**, *153*, A2103−A2110.

(9) Fornasari, G.; Gusi, S.; Trifiro, F.; Vaccari, A. Cobalt Mixed Spinels as Catalysts for the Synthesis of Hydrocarbons. *Ind. Eng. Chem. Res.* **1987**, *26*, 1500−1505.

(10) Volkova, G.; Yurieva, T.; Plyasova, L.; Naumova, M.; Zaikovskii, V. Role of the Cu−Co Alloy and Cobalt Carbide in Higher Alcohol Synthesis. *J. Mol. Catal. Chem.* **2000**, *158*, 389−393.

(11) Singh, D. J. Electronic and Thermoelectric Properties of $CuCoO_2$: Density Functional Calculations. *Phys. Rev. B* **2007**, *76*, 085110.

(12) Beekman, M.; Salvador, J.; Shi, X.; Nolas, G. S.; Yang, J. Characterization of Delafossite-Type $CuCoO_2$ Prepared by Ion Exchange. *J. Alloys Compd.* **2010**, *489*, 336−338.

(13) La Rosa-Toro, A.; Berenguer, R.; Quijada, C.; Montilla, F.; Morallón, E.; Vázquez, J. L. Preparation and Characterization of Copper-Doped Cobalt Oxide Electrodes. *J. Phys. Chem. B* **2006**, *110*, 24021−24029.

(14) Jia, J.; Li, X.; Chen, G. Stable Spinel Type Cobalt and Copper Oxide Electrodes for $O_2$ and $H_2$ Evolutions in Alkaline Solution. *Electrochim. Acta* **2010**, *55*, 8197−8206.

(15) Singh, R. N.; Pandey, J. P.; Singh, N. K.; Lal, B.; Chartier, P.; Koenig, J.-F. Sol-gel Derived Spinel $M_xCo_{3-x}O_4$ (M = Ni, Cu; 0 ≤ x ≤ 1) Films and Oxygen Evolution. *Electrochim. Acta* **2000**, *45*, 1911−1919.

(16) Hamid, M.; Tahir, A. A.; Mazhar, M.; Molloy, K. C.; Kociok-Köhn, G. Copper−Cobalt Heterobimetallic Ceramic Oxide Thin Film Deposition: Synthesis, Characterization and Application of Precursor. *Inorg. Chem. Commun.* **2008**, *11*, 1159−1161.

(17) Shaheen, W. M.; Ali, A. A. Characterization of Solid−Solid Interactions and Physico-Chemical Properties of Copper−Cobalt Mixed Oxides and $Cu_xCo_{3-x}O_4$ Spinels. *Mater. Res. Bull.* **2001**, *36*, 1703−1716.

(18) Leyland, A.; Matthews, A. On the Significance of the H/E Ratio in Wear Control: A Nanocomposite Coating Approach to Optimised Tribological Behaviour. *Wear* **2000**, *246*, 1−11.

(19) Zhang, F. C.; Luo, H. H.; Wang, T. S.; Roberts, S. G.; Todd, R. I. Influence Factors on Wear Resistance of Two Alumina Matrix Composites. *Wear* **2008**, *265*, 27−33.

(20) Hongbing Liu, J. T. Corrosion and Tribological Behaviors of Chromium Oxide Coatings Prepared by the Glow-Discharge Plasma Technique. *Surf. Coat. Technol.* 28−36.

(21) Freyman, C. A.; Chung, Y.-W. Synthesis and Characterization of Hardness-Enhanced Multilayer Oxide Films for High-Temperature Applications. *Surf. Coat. Technol.* **2008**, *202*, 4702−4708.

(22) Amri, A.; Jiang, Z.-T.; Pryor, T.; Yin, C.-Y.; Xie, Z.; Mondinos, N. Optical and Mechanical Characterization of Novel Cobalt-Based Metal Oxide Thin Films Synthesized Using Sol−Gel Dip-Coating Method. *Surf. Coat. Technol.* **2012**, *207*, 367−374.

(23) Amri, A.; Duan, X.; Yin, C.-Y.; Jiang, Z.-T.; Rahman, M. M.; Pryor, T. Solar Absorptance of Copper−Cobalt Oxide Thin Film Coatings with Nano-Size, Grain-Like Morphology: Optimization and Synchrotron Radiation XPS Studies. *Appl. Surf. Sci.* **2013**, *275*, 127−135.

(24) Oliver, W. C.; Pharr, G. M. Measurement of Hardness and Elastic Modulus by Instrumented Indentation: Advances in Understanding and Refinements to Methodology. *J. Mater. Res.* **2004**, *19*, 3−20.

(25) Zhao, X.; Xie, Z.; Munroe, P. Nanoindentation of Hard Multilayer Coatings: Finite Element Modelling. *Mater. Sci. Eng.* **2011**, *528*, 1111−1116.

(26) Li, Z.; Munroe, P.; Jiang, Z.; Zhao, X.; Xu, J.; Zhou, Z.; Jiang, J.; Fang, F.; Xie, Z. Designing Superhard, Self-Toughening CrAlN Coatings Through Grain Boundary Engineering. *Acta Mater.* **2012**, *60*, 5735−5744.

(27) Stefanov, P.; Avramova, I.; Stoichev, D.; Radic, N.; Grbic, B.; Marinova, T. Characterization and Catalytic Activity of Cu-Co Spinel Thin Films Catalysts. *Appl. Surf. Sci.* **2005**, *245*, 65−72.

(28) Gautier, J. L.; Rios, E.; Gracia, M.; Marco, J. F.; Gancedo, J. R. Characterization by X-Ray Photoelectron Spectroscopy of Thin $Mn_xCo_{3-x}O_4$ (1 > $x$ > 0) Spinel Films Prepared by Low-Temperature Spray Pyrolysis. *Thin Solid Films* **1997**, *311*, 51−57.

(29) Petrov, K.; Markov, L. Preparation of Copper-Cobalt Oxide Spinels by Thermal Decomposition of Copper-Cobalt Basic Nitrate Mixed Crystals. *J. Mater. Sci.* **1985**, *20*, 1211−1214.

(30) Brandhorst, M.; Zajac, J.; Jones, D. J.; Rozière, J.; Womes, M.; Jimenez-López, A.; Rodríguez-Castellón, E. Cobalt-, Copper- and Iron-Containing Monolithic Aluminosilicate-Supported Preparations for Selective Catalytic Reduction of NO with NH3 at Low Temperatures. *Appl. Catal. B, Environ.* **2005**, *55*, 267−276.

(31) Xu, J.; Gao, P.; Zhao, T. S. Non-Precious $Co_3O_4$ Nano-Rod Electrocatalyst for Oxygen Reduction Reaction in Anion-Exchange Membrane Fuel Cells. *Energy Environ. Sci.* **2012**, *5*, 5333−5339.

(32) Amadelli, R.; Samiolo, L.; Maldotti, A.; Molinari, A.; Valigi, M.; Gazzoli, D. Preparation, Characterization, and Photocatalytic Behaviour of $Co-TiO_2$ with Visible Light Response. *Int. J. Photoenergy* **2008**, *2008*, 1−9.

(33) Chuang, T. J.; Brundle, C. R.; Rice, D. W. Interpretation of the X-Ray Photoemission Spectra of Cobalt Oxides and Cobalt Oxide Surfaces. *Surf. Sci.* **1976**, *59*, 413−429.

(34) Tyuliev, G.; Panayotov, D.; Avramova, I.; Stoichev, D.; Marinova, T. Thin-Film Coating of Cu-Co Oxide Catalyst on Lanthana/Zirconia Films Electrodeposited on Stainless Steel. *Mater. Sci. Eng., C* **2003**, *23*, 117−121.

(35) Tyuliev, G.; Angelov, S. The Nature of Excess Oxygen in $Co_3O_4+\varepsilon$. *Appl. Surf. Sci.* **1988**, *32*, 381−391.

(36) Peng, Y.-Y.; Hsieh, T.-E.; Hsu, C.-H. White-Light Emitting $ZnO-SiO_2$ Nanocomposite Thin Films Prepared by the Target-Attached Sputtering Method. *Nanotechnology* **2006**, *17*, 174−180.

(37) Dupin, J.-C.; Gonbeau, D.; Vinatier, P.; Levasseur, A. Systematic XPS Studies of Metal Oxides, Hydroxides and Peroxides. *Phys. Chem. Chem. Phys.* **2000**, *2*, 1319−1324.

(38) Royer, S.; Van Neste, A.; Davidson, R.; McIntyre, S.; Kaliaguine, S. Methane Oxidation Over Nanocrystalline $LaCo_{1-x}Fe_xO_3$: Resistance to $SO_2$ Poisoning. *Ind. Eng. Chem. Res.* **2004**, *43*, 5670−5680.

(39) Hähner, G. Near Edge X-Ray Absorption Fine Structure Spectroscopy as a Tool To Probe Electronic and Structural Properties of Thin Organic Films and Liquids. *Chem. Soc. Rev.* **2006**, *35*, 1244−1255.

(40) Lewandowski, B.; Lusker, K.; LeJeune, Z.; Lytle, D.; Zhou, P.; Sprunger, P.; Garno, J. Impact of pH, Dissolved Inorganic Carbon, and Polyphosphates for the Initial Stages of Water Corrosion of Copper Surfaces Investigated by AFM and NEXAFS. *CheM* **2011**, *1*, 16−26.

(41) Buckley, A. N.; Skinner, W. M.; Harmer, S. L.; Pring, A.; Fan, L.-J. Electronic Environments in Carrollite, $CuCo_2S_4$, Determined by Soft X-Ray Photoelectron and Absorption Spectroscopy. *Geochim. Cosmochim. Acta* **2009**, *73*, 4452−4467.

(42) Van der Laan, G.; Pattrick, R. A. D.; Henderson, C. M. B.; Vaughan, D. J. Oxidation State Variations in Copper Minerals Studied with Cu 2p X-Ray Absorption Spectroscopy. *J. Phys. Chem. Solids* **1992**, *53*, 1185−1190.

(43) Van der Laan, G.; Pattrick, R. A. D.; Charnock, J. M.; Grguric, B. A. Cu $L_{2,3}$ X-Ray Absorption and the Electronic Structure of Nonstoichiometric $Cu_5FeS_4$. *Phys. Rev. B* **2002**, *66*, 045104.

(44) Pattrick, R. A. D.; Vanderlaan, G.; Vaughan, D. J.; Henderson, C. M. B. Oxidation State and Electronic Configuration Determination of Copper in Tetrahedrite Group Minerals by L-Edge X-Ray Absorption Spectroscopy. *Phys. Chem. Miner.* **1993**, *20*, 395−401.

(45) Pattrick, R. A. D.; Mosselmans, J. F. W.; Charnock, J. M.; England, K. E. R.; Helz, G. R.; Garner, C. D.; Vaughan, D. J. The Structure of Amorphous Copper Sulfide Precipitates: An X-Ray Absorption Study. *Geochim. Cosmochim. Acta* **1997**, *61*, 2023−2036.

(46) Chen, J. G. NEXAFS Investigations of Transition Metal Oxides, Nitrides, Carbides, Sulfides and Other Interstitial Compounds. *Surf. Sci. Rep.* **1997**, *30*, 1−152.

(47) Abbate, M.; Fuggle, J. C.; Fujimori, A.; Tjeng, L. H.; Chen, C. T.; Potze, R.; Sawatzky, G. A.; Eisaki, H.; Uchida, S. Electronic Structure and Spin-State Transition of $LaCoO_3$. *Phys. Rev. B* **1993**, *47*, 16124−16130.

(48) Kroll, T.; Aligia, A. A.; Sawatzky, G. A. Polarization Dependence of X-Ray Absorption Spectra of $Na_XCoO_2$: Electronic Structure from Cluster Calculations. *Phys. Rev. B* **2006**, *74*, 115124.

(49) Van der Laan, G.; Thole; Sawatzky; Verdaguer, M. Multiplet Structure in the $L_{2,3}$ X-Ray Absorption Spectra: A Fingerprint for High- and Low-Spin $Ni^{2+}$ Compounds. *Phys. Rev. B Condens. Matter* **1988**, *37*, 6587−6589.

(50) Mizokawa, T.; Tjeng, L. H.; Steeneken, P. G.; Brookes, N. B.; Tsukada, I.; Yamamoto, T.; Uchinokura, K. Photoemission and X-Ray Absorption Study of Misfit-Layered (Bi,Pb)-Sr-Co-O Compounds: Electronic Structure of a Hole-Doped Co-O Triangular Lattice. *Phys. Rev. B* **2001**, *64*, 115104.

(51) Gautam, S.; Thakur, P.; Chae, K. H.; Chang, G. S.; Subramanain, M.; Jayavel, R. Electronic Structure of Co-doped ZnO Thin Films by X-ray Absorption and Emission Spectroscopy. *J. Korean Phys. Soc.* **2009**, *55*, 167.

(52) Singh, A. P.; Kumar, R.; Thakur, P.; Brookes, N. B.; Chae, K. H.; Choi, W. K. NEXAFS and XMCD Studies of Single-Phase Co Doped ZnO Thin Films. *J. Phys.: Condens. Matter* **2009**, *21*, 185005.

(53) Guo, J. H.; Vayssieres, L.; Persson, C.; Ahuja, R.; Johansson, B.; Nordgren, J. Polarization-Dependent Soft-X-Ray Absorption of Highly Oriented ZnO Microrod Arrays. *J. Phys.-Condens. Matter* **2002**, *14*, 6969−6974.

(54) Kenfaui, D.; Chateigner, D.; Gomina, M.; Noudem, J. G. Texture, Mechanical and Thermoelectric Properties of $Ca_3Co_4O_9$ Ceramics. *J. Alloys Compd.* **2010**, *490*, 472−479.

(55) Mammeri, F.; Bourhis, E. L.; Rozes, L.; Sanchez, C. Mechanical Properties of Hybrid Organic-Inorganic Materials. *J. Mater. Chem.* **2005**, *15*, 3787−3811.

(56) Kenfaui, D.; Bonnefont, G.; Chateigner, D.; Fantozzi, G.; Gomina, M.; Noudem, J. G. $Ca_3Co_4O_9$ Ceramics Consolidated by SPS Process: Optimisation of Mechanical and Thermoelectric Properties. *Mater. Res. Bull.* **2010**, *45*, 1240−1249.

(57) Tilbrook, M. T.; Paton, D. J.; Xie, Z.; Hoffman, M. Microstructural Effects on Indentation Failure Mechanisms in TiN Coatings: Finite Element Simulations. *Acta Mater.* **2006**, *55*, 2489−2501.